Intranuclear cascade model for 50-MeV-region (p, p′ x) reactions over a wide target mass range

Uozumi, Yusuke
Department of Applied Quantum Physics and Nuclear Engineering, Kyushu University

Yamada, Takahiro
Department of Applied Quantum Physics and Nuclear Engineering, Kyushu University

Nakano, Masahiro
Faculty of Health Sciences, Junshin Gakuen University

出版情報：Journal of Nuclear Science and Technology. 52 (2), pp.264-273, 2015. 日本原子力学会
バージョン：

Intranuclear cascade model for 50-MeV-region (p, $p'x$) reactions over a wide target mass range

Yusuke Uozumi[1]*, Takahiro Yamada[1] and Masahiro Nakano[2]

[1]*Department of Applied Quantum Physics and Nuclear Engineering, Kyushu University, 744 Motooka, Nishi-ku, Fukuoka 819-0395, Japan;* [2]*Junshin Gakuen University, 1-1-1 Chikushigaoka, Minami-ku, Fukuoka 815-8510, Japan;*

In our previous study, the applicable range of the intranuclear cascade model was successfully extended to lower incident energy (p, $p'x$) reactions by introducing trajectory deflections and low-energy-loss process due to collective excitations. However, the model's validity was confirmed only for a ^{56}Fe target. In the present work we widen the applicable range of masses of the target nucleus. First, we derive an expression for the response function, which gives the probability of collective excitation strengths, to fit the distorted-wave Born approximation results as a function of the target mass number and the beam energy. Second, the barrier transmission coefficient was investigated. An expression with a modified Gamow penetration factor was chosen from four phenomenological forms of one-dimensional barrier transmission coefficients. Calculations with the proposed model followed by a generalized evaporation model were carried out for double-differential cross sections of (p, $p'x$) reactions at 30-60 MeV. Although the response function and the transmission coefficient were only parameterized approximately, the proposed model showed good agreements with experimental observations for a variety of nuclear targets from ^{12}C to ^{209}Bi.

Keywords: intranuclear cascade model; $(p,\ p'x)$ ***reactions; collective excitation; barrier transmission coefficient; double-differential cross sections***

*Corresponding author. Email: uozumi@nucl.kyushu-u.ac.jp

1. Introduction

The intranuclear cascade (INC) model is a powerful method for describing nucleon-nucleus spallation reactions and INC algorithms are incorporated in particle transport simulations, which are used for a variety of applications. For instance, we have developed the INC-ELF code[1], which is included in the PHITS transport code[2]. Extensive effort has been devoted by many authors[1,3–11] to improve the prediction accuracy of the INC model and extend the applicable range of nuclear reactions. Although the model is believed to be valid for incident proton energies above a few hundred MeV, lowering the energy regime is of great importance for particle transport simulations. Recent papers[3, 8, 11] have reported that, although the predictive power of the INC model becomes poorer with decreasing incident energy, it is still reasonable for energies of several tens of MeV.

We have previously succeeded in extending the low-energy range of $(p,\ p'x)$ reactions that can be described by the INC model to $30 - 60$ MeV [12] by introducing two improvements: curved trajectories for energetic particles and low-energy transfers from the incident proton to the target nucleus. Although the standard INC model assumes straight trajectories, the influence of the nuclear potential cannot be ignored at low energies. It has been reported[8] that a classical particle motion needs to be modified by including refraction or reflection to explain the large angle scattering. However, we employed a Monte Carlo method of trajectory deflection with an angular probability distribution for proton-nucleus elastic scattering. The second improvement came from a speculation that the classical treatment of Pauli blocking in INC might be invalid for low-energy transfers, which govern direct reaction mechanisms. Since direct reactions leading to collective excitations dominate excitation spectra up to 10 MeV and continue to about 20 MeV, they are negligible in reactions above 200 MeV but significant below 100 MeV. To describe low-energy transfer processes, we introduced proton-nucleus response functions, which provide probabilities for populating collective excitation states in $(p,\ p')$ reactions. This model

is called the ICTC (INC with trajectory deflection and collective excitations) model in this article. The model agreed well with the experimental double-differential cross section (DDX) spectra of the inclusive ^{56}Fe$(p,\ p'x)$ reaction at 29.9 and 61.5 MeV. However, it is necessary to verify the applicability of the model to other target nuclei.

In the ICTC model, the trajectory of the proton is deflected according to the angular distribution of proton-nucleus elastic scattering when the proton passes through the nuclear surface. The angular distribution function is determined as a function of the target mass and proton energy[13].

Response functions for collective excitations need to be expressed in a general form. Collective excitations are classified into two modes: low-energy vibrational excitations (LE) and high-energy giant quadrupole resonance (GQR) excitations. Strength distribution functions were introduced into the ICTC model to treat the excitations as the energy-differential cross sections $d\sigma_{LE}/d\varepsilon$ and $d\sigma_{GQR}/d\varepsilon$. In principle, these excitations should depend strongly on the nature of the target nucleus. However, the relative strengths of these excitations may not be very large in terms of the entire energy spectrum of the inclusive $(p,\ p'x)$ reactions, and a rough estimate may improve the accuracy greatly. To use the ICTC model for many target nuclei, it is essential to identify trends in the strength distributions of these excitations.

Our first study of the ICTC model focused on only ^{56}Fe targets and thus did not consider barrier transmission. However, the ICTC model must treat the barrier effect carefully for low-energy proton emission from a heavy nucleus, as a heavy target nucleus has a high barrier due to the Coulomb and centrifugal forces. After the pioneering studies by Blatt and Weisskopf[14] and Preston[15], barrier transmission has been studied by many researchers in terms of a static one-dimensional barrier. Depending on reaction type and expected accuracy of calculations, some theoretical methods have been developed to include, for instance, barrier fluctuation[16, 17], multidimensional potential[18],

and multi-humped fission barriers[19]. A treatment for fission involved the dynamic evolution of a system along a complicated energy surface depending on the deformation of the nucleus[20]. In general, however, a one-dimensional barrier penetration model formulated with the Fermi function is satisfactory for many experimental observations. The phenomenological Hill-Wheeler formula is also in the form of the Fermi function[21] and can be used to analyze particle evaporation from heavy-ion incident compound reactions at energies of 10 MeV/nucleon or less[22–24]. At incident energies above the barrier[25], transmission coefficients can be determined from optical potentials for light projectiles and then expressed by a slightly modified Hill-Wheeler formula. The Gamow penetration factor is also successful in explaining alpha decay. The barrier effect is only roughly approximated in the standard INC model because the model is used for reactions with beam energies greater than several hundred megaelectron volts. For such high energies, the barrier energy domain occupies a negligible part of the entire energy spectrum. Evaporation models used with INC models also approximate the barrier. For example, the generalized evaporation model (GEM)[26, 27] uses a simple function for the Coulomb barrier transmission to describe total reaction cross sections. In this paper, we will examine these one-dimensional penetration models and determine the best function and the values of its parameters by comparing ICTC results with experimental data.

In the present study, we expand the domain of applicability of the ICTC model to inclusive $(p,\ p'x)$ reactions for a wide mass range of target nuclei and beam energies from 30 to 60 MeV. We intend to provide an approximate overview of the general behavior of the barrier transmission coefficient and the collective excitation response function. These two quantities are not treated explicitly by not only INC but also other existing models, for instance FKK[28], TUL[29], and SCDW[30, 31]. Therefore, another purpose of this work is to obtain the deeper insight of inclusive $(p,\ p'x)$ reactions with the ICTC model. Although the spectral shape of threshold energies is strongly affected by the evaporation

of particles, the evaporation stage is beyond the scope of our study. The rest of this paper is organized as follows. In Section II, the basic ICTC model is described. In Section III, the strength distribution functions of the collective excitations are introduced, the mass and energy dependence of the low-energy excitations are investigated, and the transmission coefficient is discussed. In Section IV, the proposed model is validated by comparing the results with experimental data over a wide range of target nuclei masses.

2. Model

We have previously published the details of the ICTC model and the calculation procedures[12], so we will only outline them here. The spin-isospin degrees of freedom are ignored to simplify expressions. The ICTC model assumes that the DDXs of the $(p,\ p'x)$ reactions are given by

$$\frac{d^2\sigma}{dEd\Omega} = \sigma_{total}\frac{1}{2\pi\Delta E\Delta\cos(\theta)}\sum_k P^k(\theta,\varepsilon), \tag{1}$$

where ΔE and $\Delta\cos\theta$ are the bin widths of the outgoing energy, ε, and the emission angle, θ, respectively. σ_{total} is the proton-nucleus total cross section. With an assumption that the collective excitation occurs at the nuclear surface of entrance channel, the nonperturbative form of proton emission probability P^{np} is expressed as

$$P^{np}(\theta,\varepsilon) = P_{def}^{\varepsilon_0;in}(\theta_{in},t_1)\left(1+P_{co}\left(\theta_{co},\varepsilon_{co},t_2\right)\right)\left(\Gamma+G_{cas}\left(\theta_{cas},\varepsilon_{cas}\right)\right)T_c(\varepsilon)P_{def}^{\varepsilon;ex}(\theta_{ex},t_{ex}) \tag{2}$$

for

$$G_{cas}(\theta,\varepsilon) = \Gamma P_{nc}(\theta_{m1},\varepsilon_{m1},t_{m1})\Gamma + \Gamma P_{nc}(\theta_{m2},\varepsilon_{m2},t_{m2})\Gamma P_{nc}(\theta_{m3},\varepsilon_{m3},t_{m3})\Gamma+\cdots,$$

with time order defined by

$$0<t_1<t_2<\cdots<t_{m1}<t_{m2}<\cdots<t_{ex}.$$

The proton enters and outgoes the target nucleus at time t_1 and t_{ex}, respectively. In the equation, scripts are used to identify the process. Γ is the space development operator for an energetic nucleon with velocity $\boldsymbol{v}$ and is written as

$$\Gamma(\boldsymbol{r}, \boldsymbol{r}') : \boldsymbol{r} \rightarrow \boldsymbol{r}' = \boldsymbol{r} + \boldsymbol{v}t;$$

$$\forall t > 0, r' < R_{max}, p > p_F,$$

where R_{max} is the maximum nuclear radius, and p_F is the Fermi momentum. The expression of P^{np} for the standard INC model is given by

$$P^{np} = G_{cas}.$$

The probability of deflection angle θ at the nuclear surface is assumed to be

$$P^{\varepsilon}_{def}(\theta) = \frac{\sin\theta}{\sigma^{\varepsilon}_{el}} \frac{d\sigma^{\varepsilon}_{el}}{d\Omega}(\theta), \tag{3}$$

where $\sigma^{\varepsilon}_{el}$ is the proton-nucleus elastic scattering cross section. The assumption to use the elastic scattering angular distribution is discussed in the next section. In the case of a single-interaction (one-step) reaction, the probabilities of collective excitation, P_{co}, and noncollective excitation, P_{nc}, are

$$P_{co}(\varepsilon) = \frac{1}{\sigma_{\,total}} \frac{d\sigma_{co}}{d\varepsilon} \delta(E_{in} - \varepsilon - Ex_{co}), \tag{4}$$

$$P_{nc}(\theta, \varepsilon) = Q \frac{\rho(\boldsymbol{r}) \Delta r^3}{A \sigma_{NN}} \left(\int_{p<p_F} \frac{d\sigma_{NN}}{d\Omega} dp \right)_{\theta} \delta(E_{in} - \varepsilon - Ex_{nc}), \tag{5}$$

where σ_{co} is the proton-nucleus cross section of collective excitations, E_{in} is the incoming energy, and Ex is the excitation energy. It is assumed that $\frac{d\sigma_{co}}{d\varepsilon}$ is given by the incoherent sum of the cross sections of two excitations:

$$\frac{d\sigma_{co}}{d\varepsilon} = \frac{d\sigma_{LE}}{d\varepsilon} + \frac{d\sigma_{GQR}}{d\varepsilon}. \tag{6}$$

In Ref.[32], the NN cross section, σ_{NN}, and its angular distributions are parameterized. ρ and Δr^3 represent the nuclear density and a minute volume, respectively. The projection

operator, Q, for the Pauli blocking is

$$Q|ij\rangle = \begin{cases} |ij\rangle & \text{When both particles } i \text{ and } j \text{ are above the Fermi surface.} \\ 0 & \text{otherwise.} \end{cases} \quad (7)$$

In this study, Eq. (2) includes the transmission coefficient, T_c, which was disregarded in Eq. (22) of Ref.[12]. We considered T_c for only the exit channel, because it is negligible at the entrance channel in this beam energy range. T_c is discussed in detail in section III-C.

The angular distribution of the elastic scattering has been parameterized[13] as a function of proton energy and target mass as

$$\frac{d\sigma_{el}}{d\Omega}(\varepsilon, A, \theta) = N \exp[-0.001(1.3\varepsilon + 6 \ln A - 5)\theta], \quad (8)$$

where N is a normalization factor. Units of ε and θ are in megaelectron-volts and degrees, respectively. This underestimates the cross sections for most forward angles where the Coulomb repulsive force dominates because the incident proton will pass the target nucleus at a very large impact parameter value and not contribute to nuclear reactions. It is assumed that only the deflection caused by the attractive force influences the nuclear reactions. Although the diffraction pattern is disregarded, this distribution function has proved useful in ICTC calculations of continuum DDX spectra.

The numerical calculation is carried out using the Monte Carlo method in order to follow the time development of the nuclear system[12, 33]. The initial state provides all the nucleon coordinates in phase space. The target nucleons are given random positions and momenta in agreement with the Woods-Saxon and Fermi sphere distributions, respectively. The nuclear radius in femtometers is defined[34] by $r_0 = (0.976 + 0.0206A^{1/3})A^{1/3}$. The maximum nuclear radius is given by $R_{max} = r_0 + 4a_0$, where a_0 is the diffuseness, which is set to 0.54 fm. The projectile proton is randomly assigned an impact parameter value in the range 0–R_{max}.

Over time, the energetic particles move along straight lines in the nucleus. The intranuclear NN collisions are assumed to take place when two nucleons approach each

other at a distance of less than $\sqrt{\sigma_{NN}/\pi}$. When an energetic nucleon hits the nuclear surface, it can be reflected by the potential barrier or it can penetrate the barrier, depending on the transmission coefficient. The reflected nucleon is assumed to be bound in a compound state, and it does not escape during the cascade phase.

When the cascade phase is finished, further particle emission may occur during the evaporation process which we simulate using the GEM in this study. The GEM is based on the Weisskopf-Ewing model[35, 36] and assumes an isotropic angular distribution of particle emission in the center-of-mass system for neutrons and charged particles. It must be noted that experimentally observed angular distributions are not isotropic for charged particle emission[14, 15, 37, 38].

3. Parameterization

3.1. High-energy Collective Excitation

The strength distribution of GQR is accurately expressed by the Breit-Wigner distribution as a function of the excitation energy, Ex,

$$\frac{d\sigma_{GQR}}{d\varepsilon}(Ex) = S_{GQR}\frac{1}{\pi}\frac{(\Gamma_{GQR}/2)^2}{(E_{GQR}-Ex)^2+(\Gamma_{GQR}/2)^2}, \tag{9}$$

where σ_{GQR} is the GQR cross section, S_{GQR} is a normalization factor, E_{GQR} is the average excitation energy of the resonance, and Γ_{GQR} is the resonance width. In the present work we use the following parameter values, which were reported in Ref.[12], for the ^{56}Fe(p, $p'x$) reactions.

$$\sigma_{GQR} = 0.065\sigma_{total},$$

$$\Gamma_{GQR} = 8 \quad (MeV),$$

and

$$E_{GQR} = 65A^{-1/3} \quad (MeV).$$

We assumed the total cross section, σ_{total}, is the same as the geometrical cross section, πR^2_{max}.

3.2. Low-energy Collective Excitation

The strengths were calculated using the distorted-wave Born approximation (DWBA) with the CCONE code[39]. The deformation parameter values for proton inelastic scattering were taken from the Evaluated Nuclear Structure Data File database[40]. The strength distributions were fitted to the Breit-Wigner distribution,

$$\frac{d\sigma_{LE}}{d\varepsilon}(Ex) = \frac{\eta S_{LE}}{\pi} \frac{(\Gamma_{LE}/2)^2}{(E_{LE} - Ex)^2 + (\Gamma_{LE}/2)^2}, \tag{10}$$

where the peak energy, E_{LE}, the width, Γ_{LE}, the absorption coefficient, η, and the cross section, σ_{LE}, are parameters. S_{LE} is a normalization factor. An example of the distribution is shown in Fig. 1 for ^{209}Bi$(p,\ p')$ at 61.7 MeV. The histogram is the strength density distribution obtained from the DWBA calculations for 17 transitions, and the broken line is the curve of Eq. (10) fitted to the histogram. The fitting was executed under the two conditions: the integrated strength conservation, and the range of strength distribution over the excitation from zero to about 10 MeV. To determine the general forms of these parameters, calculations were made for 11 targets (^{40}Ar, ^{56}Fe, ^{63}Cu, ^{74}Ge, ^{84}Kr, ^{92}Zr, ^{114}Cd, ^{120}Sn, ^{144}Nd, ^{198}Pt, and ^{209}Bi) and a wide range of beam energies. Thus, we determined the behavior of E_{LE} and Γ_{LE}:

$$E_{LE}(A) = 0.0433A^{0.807} \quad (MeV)\,, \tag{11}$$

$$\Gamma_{LE} = 3 \quad (MeV)\,. \tag{12}$$

In Fig. 2, the dependence of σ_{LE} on the incident energy, E_0, is shown for the ^{209}Bi target. The fitting result of the Breit-Wigner function is shown by the solid curve. The target mass dependence of σ_{LE} for $(p,\ p')$ reactions at $E_0 = 50$ MeV is shown in Fig. 3.

The solid curve represents the determined function of

$$\sigma_{LE}(A, E_0) = 117.88 \exp(-0.012A) \frac{50^2}{(30 - E_0)^2 + 50^2}. \tag{13}$$

The function values of Eq. (10) is shown in Fig. 1 as a solid line. Finally, the values of η were determined. Since the collective excitation strengths are lost due to the term $P_{co}G_{cas}$, η was adjusted in ICTC calculations so that the value of P_{co} term is in agreement with the integrated DWBA strength.

Its functional form was determined to be

$$\eta(A, E_0) = 0.0089A + 1.6576 - (0.0009A + 0.027) \ln E_0. \tag{14}$$

[Figure 1 about here.]

[Figure 2 about here.]

[Figure 3 about here.]

3.3. Barrier Transmission Coefficient

To express the transmission coefficient, T_c, the step function is frequently used. In our previous work we took

$$T_c^s(\varepsilon) = \begin{cases} 1 & \varepsilon > V_{Coul}, \\ 0 & \varepsilon \leq V_{Coul}, \end{cases} \tag{15}$$

with

$$V_{Coul} = \frac{e^2 Z_{target}}{R_{max}}. \tag{16}$$

We chose $R_{max} = r_0 + 4a_0$ to be large in order to maintain consistency with the low-energy cutoff used in GEM, which is discussed below. This function disregards quantum transmission, which is not an acceptable approximation here.

A widely used transmission coefficient has the Fermi-function form

$$T_c^F(\varepsilon) = \frac{1}{1 + \exp\left[-\dfrac{\varepsilon - kV_{Coul}}{d}\right]}, \tag{17}$$

where k and d are parameters. In the present work, we chose $k = 1.0$ and $d = 5.0$.

For α decays, a transmission coefficient with the Gamow penetration factor [41] is widely used. It has the form

$$T_c^G(\varepsilon) = \exp\left[-\frac{2R_{ct}}{\hbar}\frac{\sqrt{2m\varepsilon}}{E_{ct}^2}\left(\cos^{-1}E_{ct} - E_{ct}\sqrt{1-E_{ct}^2}\right)\right], \tag{18}$$

with

$$E_{ct} = \sqrt{\frac{\varepsilon}{V_{ct}}},$$

where R_{ct} is the classical turning point outside of the potential and V_{ct} is the Coulomb potential at R_{ct}. Although this equation was deduced for the barrier penetration of an S-wave particle, the present study needs T_c for a wide energy-range. For the high-energy particle, R_{ct} may become smaller in principle, and the centrifugal potential appears in addition to the Coulomb potential.

Therefore, we rewrote Eq. (18) as

$$T_c^G(\varepsilon) = \exp\left[-\frac{2\lambda_r R_{max}}{\hbar}\frac{\sqrt{2m\varepsilon}}{E_{ct}'^2}\left(\cos^{-1}E_{ct}' - E_{ct}'\sqrt{1-E_{ct}'^2}\right)\right], \tag{19}$$

with

$$E_{ct}' = \sqrt{\frac{\varepsilon}{\lambda_c V_{Coul}}},$$

where λ_r and λ_c are parameters that depend on atomic number of the target nucleus.

In the evaporation code GEM, T_c^{ev} is expressed as

$$T_c^{ev}(\varepsilon) = \begin{cases} 1 - \dfrac{V_{lt}}{\varepsilon} & \varepsilon > V_{lt}, \\ 0 & \varepsilon \le V_{lt}, \end{cases} \tag{20}$$

where V_{lt} is the Coulomb potential given by

$$V_{lt} = C_t V_{Coul}. \tag{21}$$

The value of C_t was defined in the GEM code according to Ref.[42] as the lower cutoff energy for a variety of reactions. All C_t values are smaller than unity.

Values for parameters in Eqs. (17) and (19) were found that gave the best approximations to experimental $(p,\ p'x)$ spectra under a condition of the cutoff energy

$$T_c = 0 \quad \text{for} \quad \varepsilon \leq V_{lt}, \tag{22}$$

which is same as GEM condition. Parameters were searched to keep a good continuity at the energy $\varepsilon = V_{lt}$.

As discussed in the next section, we finally decided to use the function with modified Gamow factor. Its parameter values were determined to be

$$\lambda_r(Z) = \begin{cases} -0.0055Z + 0.637 & \text{for} \quad Z > 50, \\ 0.36 & \text{for} \quad Z \leq 50, \end{cases} \tag{23}$$

and

$$\lambda_c(Z) = \begin{cases} 1.5 & \text{for} \quad Z = 79 \quad \text{and } 83, \\ 1 & \text{for} \quad Z \leq 50. \end{cases} \tag{24}$$

Because there were no experimental $(p,\ p'x)$ data for the mass range between ^{120}Sn ($Z = 50$) and ^{197}Au ($Z = 79$), a value for λ_c in this range was not obtained.

4. Calculation Results and Discussion

To validate our ICTC and GEM model, calculated DDX spectra for inclusive $(p,\ p'x)$ reactions were compared with experimental observations in Figs. $4-6$ and $8-15$. Factors indicated in these figures are multiplied to avoid overlap. The circles represent the experimental data obtained by Bertrand and Peele [43], and the numerical data were taken from Experimental Nuclear Reaction Data (EXFOR)[44]. The reported error includes statistical errors only, which are smaller than circles in the figures. The low-energy limits of data are different between 3 and 9 MeV depending on measured angle. Since they used a 0.1-mm-thick Si detector, which stops 3-MeV protons, as a transmission detector in the conventional $dE - E$ method, some of their data observed at energies below 5 MeV

showed anomalous behaviors. We therefore removed the data below 5 MeV.

Spectra in Fig. 4 show a comparison of the different transmission coefficients of Eq. (15), Eq. (17), Eq. (20) and Eq. (19) for a ^{209}Bi target with a beam energy of 61.7 MeV at laboratory angle 30°. The effect of barrier transmission is substantial in the low-energy range of the spectra. The results calculated with the step function of Eq. (15) increasingly overestimate the spectrum as proton energy decreases and then falls off steeply when the barrier energy is crossed. Results for the transmission coefficients of Eq. (17) and Eq. (20) are slightly better, but overestimation still occurs in the energy range up to 20 MeV. In contrast, calculations using the modified Gamow factor of Eq. (19) give the best approximation to the experimental data over all energies down to the threshold. The same tendency appears in other reactions, that is with different targets and beam energies. We, therefore, decided to use Eq. (19) for the transmission coefficient. All the following calculations were made using this modified Gamow factor.

[Figure 4 about here.]

In Fig. 5, DDX spectra are compared at angles from 15° to 90° for the ^{209}Bi$(p,\ p'x)$ reaction at 61.7 MeV. The totals of ICTC and GEM agree well with experiments at all angles over the whole energy range, though slight discrepancies are observed in the highest-energy and lowest-energy regions. The difference at high energies is attributed to the rough approximation of the collective excitation response function in terms of target mass. Evaporation contributions calculated with GEM are also shown in the figure. The lowest-energy regions for all angles are almost entirely determined by evaporation components, which slightly overestimate the experimental data at 90° and greatly underestimate the data at 15°.

[Figure 5 about here.]

[Figure 6 about here.]

For comparison, Fig. 6 shows the standard INC result, which includes neither trajec-

tory deflection nor collective excitation processes. The INC model appears to underestimate the higher-energy domain and overestimate for energies less than 30 MeV. The underestimations are improved by ICTC significantly in Fig. 5. Since E_{GQR} and E_{LE} are approximately 11 and 3 MeV for ^{209}Bi, the improvements at forward angles are ascribable to inclusion of the collective excitations. This argument is supported by Fig. 8, which shows the influence of collective excitations. It is supposed that the cause of improvement at the large angle (90°) is the inclusion of trajectory deflection. The peak appearing at the highest energy in ICTC results is ascribable to the inclusion of the trajectory deflection. This peak corresponds to nuclear elastic scattering, which was excluded in EXFOR. Because the kinematics of the proton-nucleus collision was not considered in the model, the energy value was incorrect. Its angular distributions are shown in Fig. 7 to be compared with the optical model calculations for ^{209}Bi$(p,\ p)$ obtained with CCONE[39]. Good agreements are observed except for forward angles. Since we disregarded the repulsive Coulomb interaction, small angle scattering is underestimated.

[Figure 7 about here.]

It is important to examine the assumption that the addition of the collective excitation cross section accompanies no expansion of the Hilbert space. Figure 8 compares the results between with and without collective excitation processes in the ^{209}Bi$(p,\ p'x)$ reaction at 61.7 MeV. Only the difference is observed at the forward angle and the highest energy portion with the excitation lower than 20 MeV. The other parts are consistent to each other. These results support our assumption.

[Figure 8 about here.]

Figure 9 shows similar comparisons to Fig. 5 for the same reaction at a beam energy of 38.7 MeV. Close agreement is obtained at all angles over the whole energy span. Evaporation events make only a small contribution, in contrast to the results for the higher incident energy of 61.7 MeV.

[Figure 9 about here.]

Figures 10 and 11 show the results for an ^{197}Au target with beam energies of 61.5 MeV and 28.8 MeV, respectively. The collective excitation regions are well fitted and the extent of agreement is better than for the ^{209}Bi target. The evaporation regime for the 61.5-MeV reaction reveals a similar tendency to that of the ^{209}Bi case, but evaporation makes a very large contribution at 50°, 75°, and 99°. In the 28.8-MeV case, reasonable agreements are observed, and GEM results are smaller than the experimental values.

[Figure 10 about here.]

[Figure 11 about here.]

Figures 12 and 13 show the DDX spectra for an ^{120}Sn target with beam energies of 61.5 and 28.8 MeV, respectively. The fits are satisfactory at the both energies; for 28.8 MeV, however, the prediction underestimates experimental results at 15° over a wide energy range. It must be noted that authors suggested that the slit scattering contribution caused enhancements of the cross section at small angles.

[Figure 12 about here.]

[Figure 13 about here.]

Figures 14 and 15 show the DDX spectra for the lighter ^{27}Al and ^{12}C targets with beams of 62 MeV. Although experimental data are scattered in the high-energy range, reflecting their shell structures, overall good fits are indicated. In these light target cases, the Coulomb barrier is very low and the contribution from evaporation is very large, as revealed for the Fe target in Ref.[12].

[Figure 14 about here.]

[Figure 15 about here.]

Results for the threshold energy regime can be summarized as follows. The modified Gamow factor was the best at expressing the transmission coefficient. For the heavy targets of ^{120}Sn, ^{197}Au, and ^{209}Bi, the evaporation contribution becomes larger with increasing

beam energy, and overestimate at 60 MeV of around 90° but a significant underestimation at 15°−20°. This implies that the GEM assumptions need to be revised. However, it should be remembered that the accuracy of the experimental data in the barrier energy region may be low.

5. Conclusion

We investigated the proton transmission coefficient and the response function of collective excitations in $(p,\ p'x)$ reactions to expand the applicable range of the INC model to a wide mass range of target nuclei at low incident energies of around 50 MeV. To determine the response function, the DWBA results were fitted as a function of target mass number and beam energy. A modified Gamow factor was chosen from four different functions as the best form for the transmission coefficient. Energy-angle distributions of $(p,\ p'x)$ reactions were calculated with the proposed model and an evaporation model. Although the response function and the transmission coefficient were only roughly determined, the calculation results agreed well with the experimental spectra on target nuclei over a wide mass range. This is the first time the transmission coefficient has been investigated quantitatively with the microscopic INC model. Further experimental data need to be obtained to improve the transmission coefficient used in this model.

References

[1] Sawada Y, Uozumi Y, Nogamine S, Yamada T, Iwamoto Y, Sato T, Niita K. Intranuclear Cascade with Emission of Light Fragment Code Implemented in the Transport Code System PHITS. Nucl. Instr. Meth. B. 2012; 291: 38-44.

[2] Sato T, Niita K, Matsuda N, Hashimoto S, Iwamoto Y, Noda S, Ogawa T, Iwase H, Nakashima H, Fukahori T, Okumura K, Kai T, Chiba S, Furuta T, Sihver L. Particle and Heavy Ion Transport Code System PHITS, Version 2.52, J. Nucl. Sci. Technol. 2013; 50:913-923.

[3] Cugnon J, Henrotte P. The low-energy limit of validity of the intranuclear cascade model. Euro. Phys. Jour. A 2003; 16: 393-407.

[4] Filges D, Goldenbaum F, Enke M, Galin JJ. Spallation neutron production and the current intranuclear cascade and transport codes. Eur. Phys. A 2001; 11:467-490.

[5] Letourneau A, Bohm A, Galin J, Lott B, Peghaire A, et al. Composite-particle emission in the reaction p+Au at 2.5 GeV. Nucl. Phys. A. 2002; 712:133-166.

[6] Mashnik SG, Gudima KK, Moskalenko IV, Prael RE, Sierk AJ. CEM2K and LAQGSM codes as event generators for space-radiation-shielding and cosmic-ray-propagation applications. Advances in Space Research 2004;34:1288-1296.

[7] Ballarini F, Battistoni G, Brugger M, Campanella M, Carboni M, et al. The physics of the FLUKA code: Recent developments. Adv. Space Res. 2007; 40:1339-1349.

[8] Duarte H. Particle production in nucleon induced reactions above 14 MeV with an intranuclear cascade model. Phys. Rev. C 2007; 75:024611.

[9] Cugnon j, Mancusi D, Boudard A, Leray S. New features of the INCL4 Model for spallation reactions. Korean Phys. Soci. 2011; 59: 955-958.

[10] Uozumi Y, Sawada Y, Mzhavia A, Nogamine S, Iwamoto H, Kin T, Hohara S, Wakabayashi G, Nakano M. Deuteron-production double-differential cross sections for 300- and 392-MeV proton-induced reactions deduced from experiment and model calculation. Phys. Rev. C 2011; 84:064617.

[11] Boudard A, Cugnon J, David JC, Leray S, Mancusi D. New potentialities of the Liege intranuclear cascade model for reactions induced by nucleons and light charged particles. Phys. Rev. C 2013; 87:014606.

[12] Uozumi Y, Yamada T, Nogamine S, Nakano M. Intranuclear cascade model including collective excitations and trajectory deflections for $(p, p'x)$ reactions around 50 MeV. Phys. Rev. C. 2012;86:034610.

[13] Yoshida H, Konishi D, Anami K, Murohka H, Uozumi Y, et al. Absolute efficiency of a stacked GSO(Ce) spectrometer for intermediate energy protons. Nucl. Inst. Meth. A 1998; 411:46-50.

[14] Blatt JM, Weisskopf VF. Theoretical Nuclear Physics. New York: John Wiley & Sons; 1952.

[15] Preston MA. Physics of the Nucleus, Addison Wesley Publishing Company; 1962.

[16] Quint AB, Reisdorf W, Schmidt K-H, Armbruster P, Hesberger FP. Investigation of the fusion of heavy nearly symmetric systems. Z. Phys. A 1993; 346:119-131.

[17] Andreyev AN, et al. Cross section systematics for the lightest Bi and Po nuclei produced in complete fusion reactions with heavy ions. Phys. Rev. C. 2005; 72: 014612.

[18] Wang C, Zhang J, Ren ZZ. Theoretical study of evaporation cross sections in the synthesis of very neutron-deficient nuclei. Phys. Rev. C. 2011; 84: 014609.

[19] Sin M, Capote R. Transmission through multi-humped fission barriers with absorption: A recursive approach. Phys. Rev. C. 2008; 77: 054601.

[20] Bjornholm S, Lynn JE. The double-humped fission barrier. Rev. Mod. Phys. 1980; 52: 725-931.

[21] Wong CY. Interaction Barrier in Charged-Particle Nuclear Reactions. 1973; 31: 766-769.

[22] Alexander JM, Guerreau D, Vaz LC. Evaporation barriers for ^{4}He indicate very extended forms for many emitting nuclei. Z. Phys. A. 1982; 305: 313-318.

[23] Huizenga JR, Behkami AN, Govil IM, Schroder WU, Toke J. Influence of rotation-induced nuclear deformation on -particle evaporation spectra. Phys. Rev. C. 1989; 40: 668-680.

[24] Sarantites DG, Baktash C, Nicolis NG, Garcia-Bermudez G, Abenante V, Beene JR, Johnson NR, et al. Nuclear-structure effects in proton evaporation spectra. Phys. Rev. Lett. 1990; 64: 2129-2132.

[25] Murthy KHN, Gupta SK, Chatterjee A. Transmission coefficients for light projectiles. Z. Phys. A.1982; 305: 73-79.

[26] Furihata S. Statistical analysis of light fragment production from medium energy proton-induced reactions. Nucl. Inst. Meth. B. 2000; 171: 251-258.

[27] Furihata S, Nakamura T. Calculation of Nuclide Productions from Proton Induced Reactions on Heavy Targets with INC/GEM. J. Nucl. Sci. Tech. Suppl. 2002; 2 :758-761.

[28] Feshbach H, Kerman A. Koonin S. The statistical theory of multi-step compound and direct reactions. Ann. Phys. 1980; 125: 429-476.

[29] Tamura T, Udagawa T, Lenske H. Multistep direct reaction analysis of continuum spectra in reactions

induced by light ions. Phys. Rev. C. 1982; 26: 379-404.

[30] Luo YL, Kawai M. Semiclassical distorted wave model of nucleon inelastic scattering to continuum. Phys. Rev. C. 1991; 43: 2367-2376.

[31] Kawai M, Weidenmüller HA. Semiclassical approximation to the two-step direct nucleon-nucleus reaction. Phys. Rev. C. 1992; 45: 1856-1862.

[32] Cugnon J, L'Hôte D, Vandermeulen J. Simple parametrization of cross-sections for nuclear transport studies up to the GeV range. Nucl. Inst. Meth. B. 1996; 111: 215-220.

[33] Iwamoto1 H, Imamura M, Koba Y, Fukui Y, Uozumi Y, et al. Proton-production double-differential cross sections for 300-MeV and 392-MeV proton-induced reactions. Phys. Rev. C. 2010; 82: 034604.

[34] Negele JW. Phys. Rev. C. Structure of Finite Nuclei in the Local-Density Approximation. 1970; 1: 1260-1321.

[35] Weisskopf VF. Statistics and Nuclear Reactions. Phys. Rev. 1937; 52: 295-303.

[36] Weisskopf VF, Ewing DH. On the Yield of Nuclear Reactions with Heavy Elements. Phys. Rev. 1940; 57: 472-485.

[37] Ericson T, Strutinski V. On angular distributions in compound nucleus processes. Nuclear Physics. 1958; 8: 284-293.

[38] Knox WJ, Quinton AR, Anderson CE. Evaporation of Charged Particles from Highly Excited Compound Nuclei. Phys. Rev. 1960; 120: 2120-2128.

[39] Iwamoto O. Development of a Comprehensive Code for Nuclear Data Evaluation, CCONE, and Validation Using Neutron-Induced Cross Sections for Uranium Isotopes. J. Nucl. Sci. Tech. 2007; 44: 687-697.

[40] Evaluated Nuclear Structure Data File. http://www.nndc.bnl.gov/ensdf/.

[41] Bowler MG. Nuclear Physics. Pergamon press; 1973. p.175-187, 272-287.

[42] Dostrovsky I, Fraenkel Z, Friedlander G. Monte Carlo Calculations of Nuclear Evaporation Processes. III. Applications to Low-Energy Reactions. Phys. Rev. 1959; 116: 683-702.

[43] Bertrand FE, Peele RW. Complete hydrogen and herium particle spectra from 30- to 60-MeV proton

bombardment of nuclei with A=12 to 209 and comparison with intranuclear cascade model. Phys. Rev. C. 1973; 8: 1045-1064.

[44] EXFOR/CSISRS Experimental Nuclear Reaction Data. http://www.nndc.bnl.gov/exfor/exfor00.htm.

Figure Captions

Figure 1 Low-energy collective excitation strengths for the ^{209}Bi($p,\ p'$) reaction at 61.7 MeV. Histogram is the DWBA result. Broken and solid curves are the Breit-Wigner distributions with parameters peculiar to this reaction and parameters of Eqs. (11) - (13), respectively.

Figure 2 The dependence of σ_{LE} on the beam energy, E_0 for ^{209}Bi($p,\ p'$) reactions.

Figure 3 The dependence of σ_{LE} on the target mass for ($p,\ p'$) reactions at 50 MeV.

Figure 4 Comparison of calculated spectra with different transmission coefficients and experimental data for the ^{209}Bi($p,\ p'x$) reaction at 61.7 MeV measured at 30°. See text.

Figure 5 Spectra of the ^{209}Bi($p, p'x$) reaction at 61.7 MeV. Circles represent experimental data. Solid and dotted lines represent calculation results for the sum of ICTC and GEM and for only GEM, respectively.

Figure 6 Same as Fig. 5 but solid lines represent calculation results for the sum of standard INC model and GEM.

Figure 7 Angular distribution of cross section of ^{209}Bi($p,\ p$) elastic scattering at 61.7 MeV. Solid and broken lines represent the calculation results with ICTC and the optical model calculation with CCONE, respectively.

Figure 8 Comparison between calculations with and without collective excitations for ^{209}Bi($p, p'x$) at 61.7 MeV. Solid and broken lines represent the

calculation results with and without, respectively.

Figure 9 Same as Fig. 5 but for the ^{209}Bi$(p, p'x)$ reaction at 38.7 MeV.

Figure 10 Same as Fig. 5 but for the ^{197}Au$(p, p'x)$ reaction at 61.5 MeV.

Figure 11 Same as Fig. 5 but for the ^{197}Au$(p, p'x)$ reaction at 28.8 MeV.

Figure 12 Same as Fig. 5 but for the ^{120}Sn$(p, p'x)$ reaction at 61.5 MeV.

Figure 13 Same as Fig. 5 but for the ^{120}Sn$(p, p'x)$ reaction at 28.8 MeV.

Figure 14 Same as Fig. 5 but for the ^{27}Al$(p, p'x)$ reaction at 62 MeV.

Figure 15 Same as Fig. 5 but for the ^{12}C$(p, p'x)$ reaction at 62 MeV.

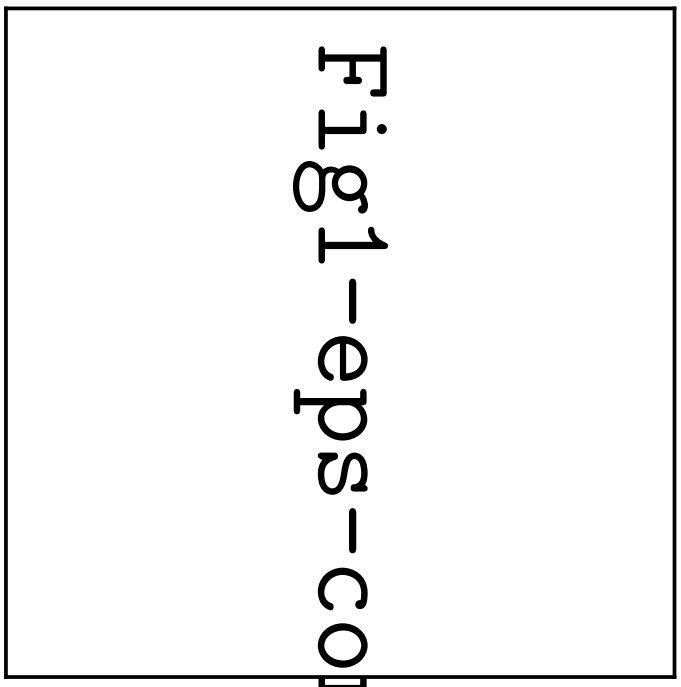

Figure 1 Low-energy collective excitation strengths for the ^{209}Bi$(p,\ p')$ reaction at 61.7 MeV. Histogram is the DWBA result. Broken and solid curves are the Breit-Wigner distributions with parameters peculiar to this reaction and parameters of Eqs. (11) - (13), respectively.

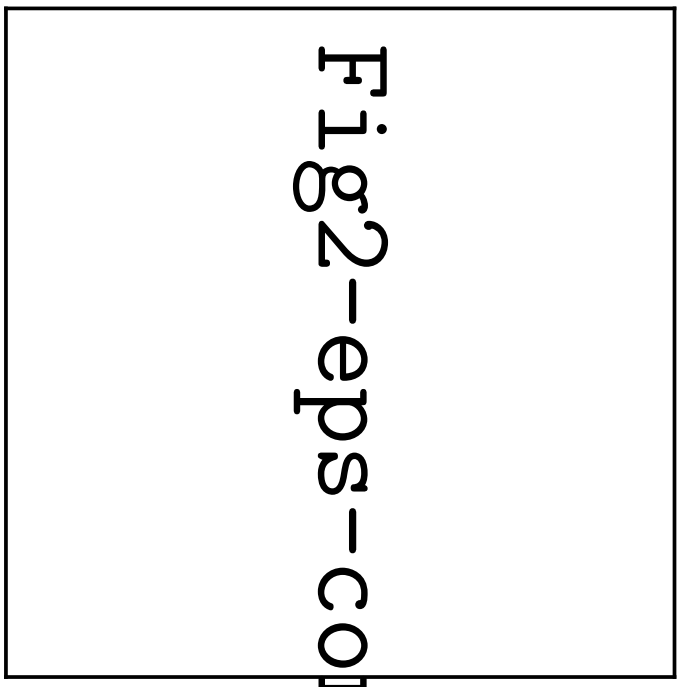

Figure 2 The dependence of σ_{LE} on the beam energy, E_0 for ^{209}Bi$(p,\ p')$ reactions.

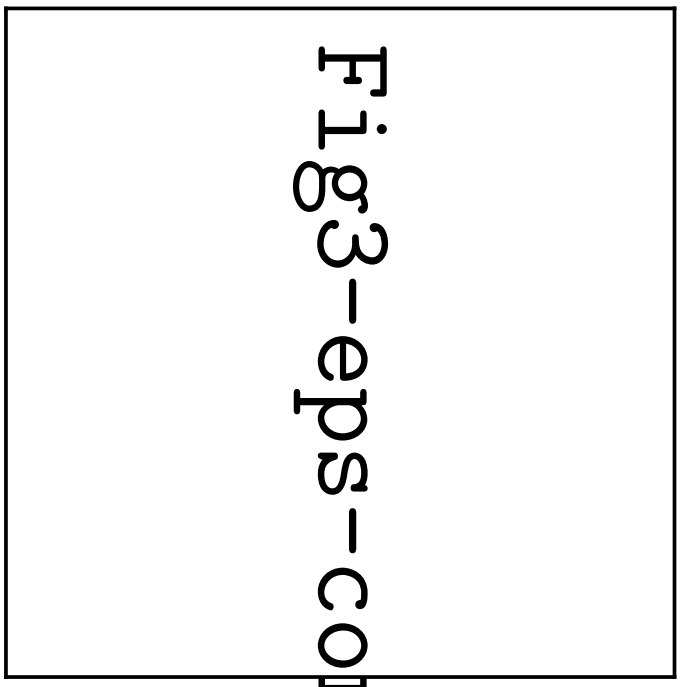

Figure 3 The dependence of σ_{LE} on the target mass for $(p,\ p')$ reactions at 50 MeV.

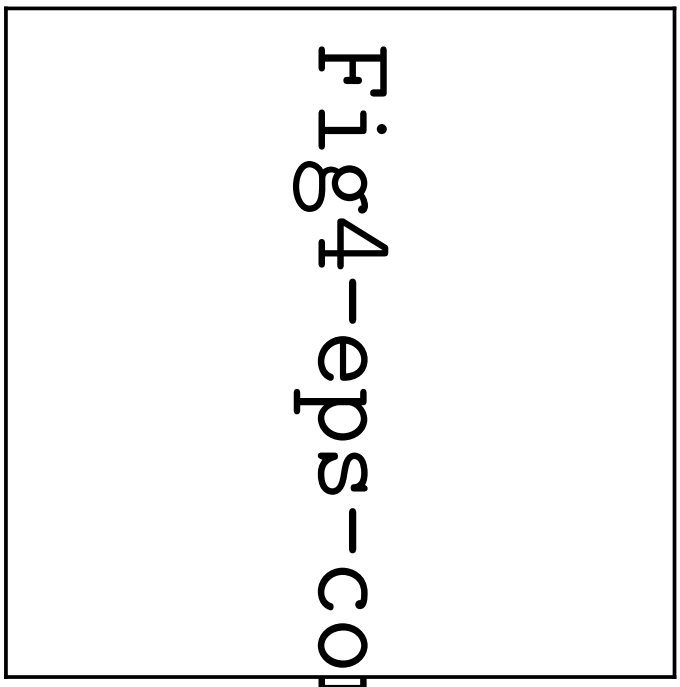

Figure 4 Comparison of calculated spectra with different transmission coefficients and experimental data for the ^{209}Bi(p, $p'\alpha$) reaction at 61.7 MeV measured at 30°. See text.

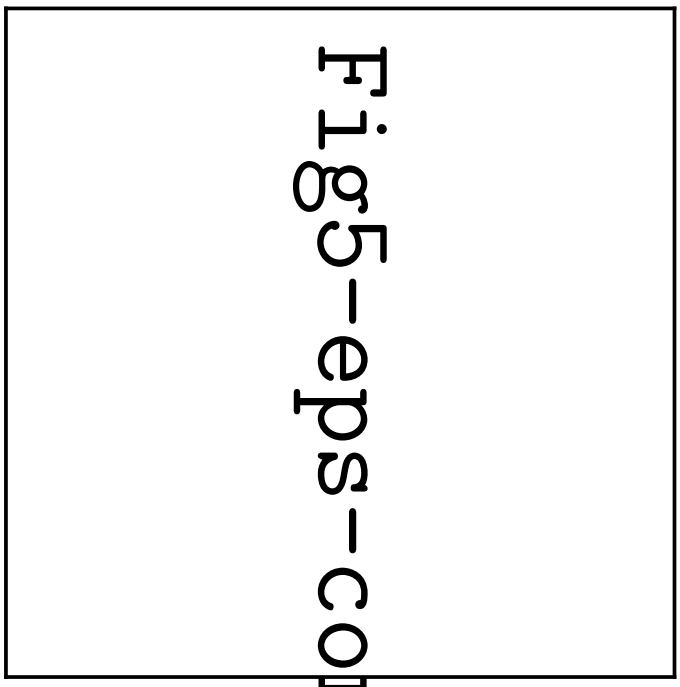

Figure 5 Spectra of the ^{209}Bi$(p, p'x)$ reaction at 61.7 MeV. Circles represent experimental data. Solid and dotted lines represent calculation results for the sum of ICTC and GEM and for only GEM, respectively.

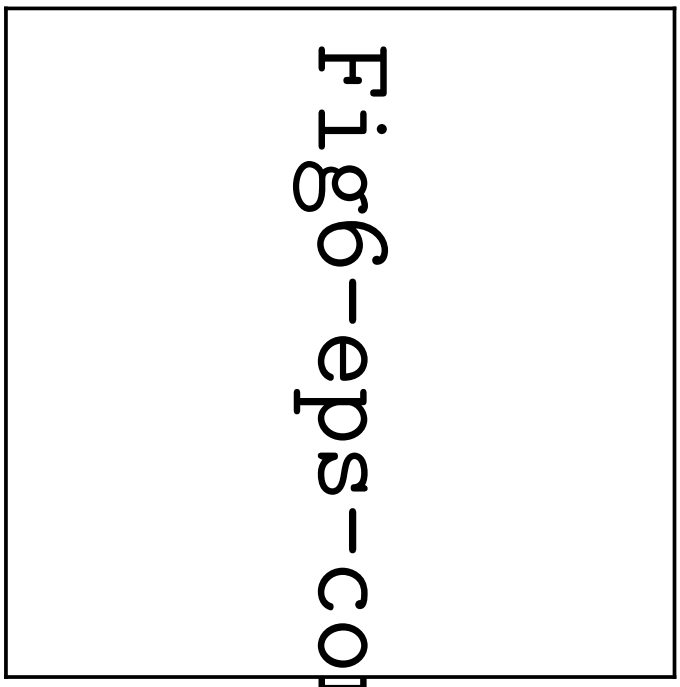

Figure 6 Same as Fig. 5 but solid lines represent calculation results for the sum of standard INC model and GEM.

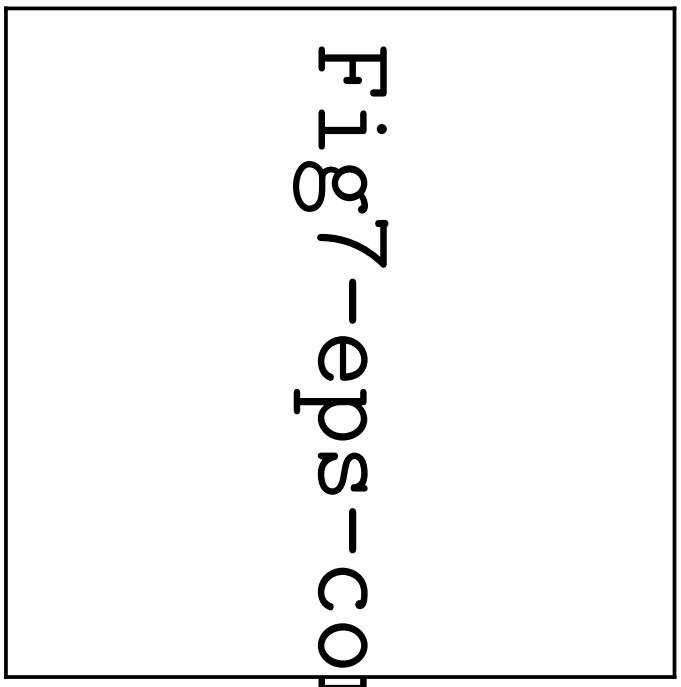

Figure 7 Angular distribution of cross section of ^{209}Bi(p, p) elastic scattering at 61.7 MeV. Solid and broken lines represent the calculation results with ICTC and the optical model calculation with CCONE, respectively.

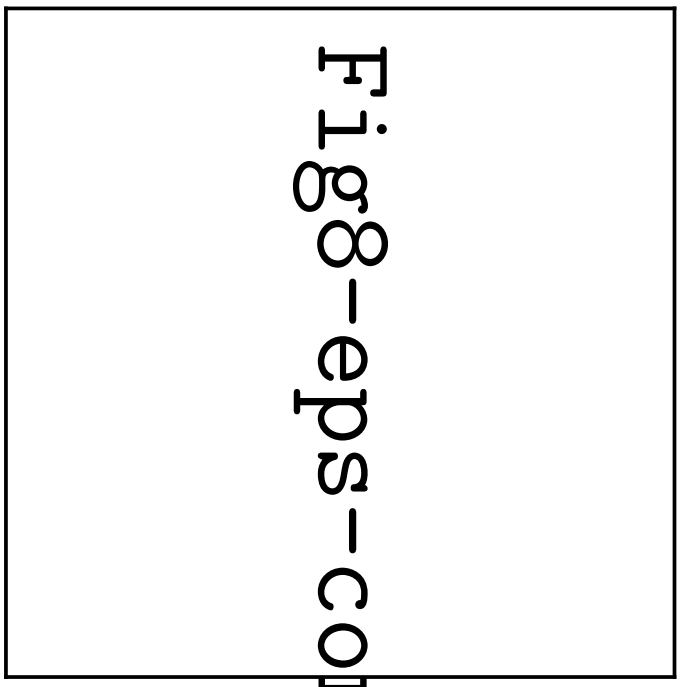

Figure 8 Comparison between calculations with and without collective excitations for ^{209}Bi$(p, p'x)$ at 61.7 MeV. Solid and broken lines represent the calculation results with and without, respectively.

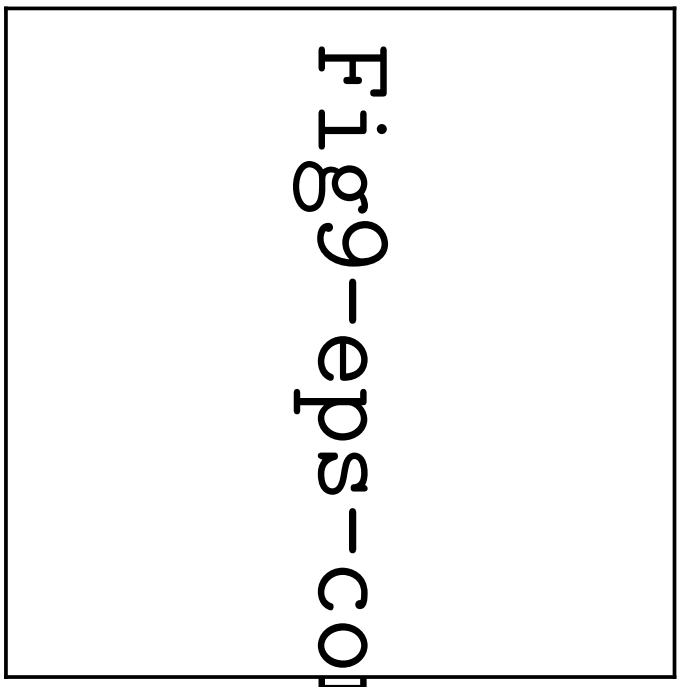

Figure 9 Same as Fig. 5 but for the ^{209}Bi$(p,p'x)$ reaction at 38.7 MeV.

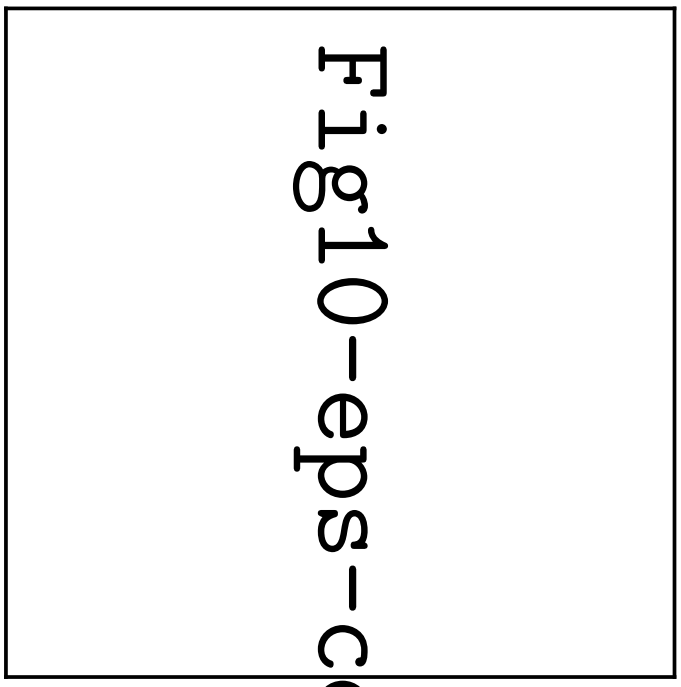

Figure 10 Same as Fig. 5 but for the ^{197}Au$(p,p'x)$ reaction at 61.5 MeV.

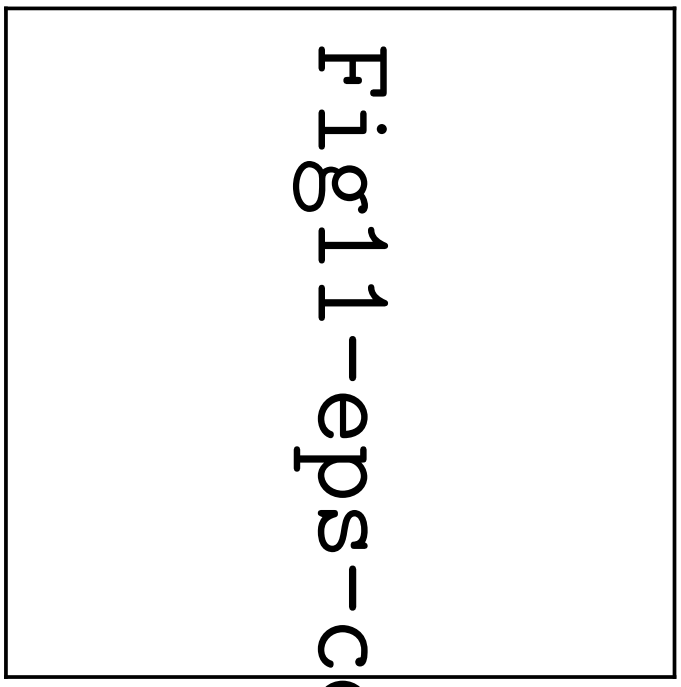

Figure 11 Same as Fig. 5 but for the ^{197}Au$(p,p'x)$ reaction at 28.8 MeV.

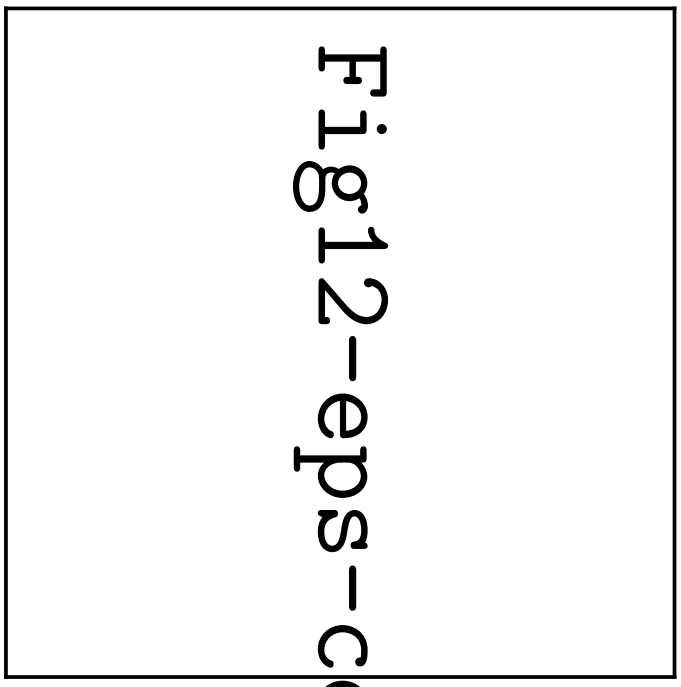

Figure 12 Same as Fig. 5 but for the ^{120}Sn$(p,p'x)$ reaction at 61.5 MeV.

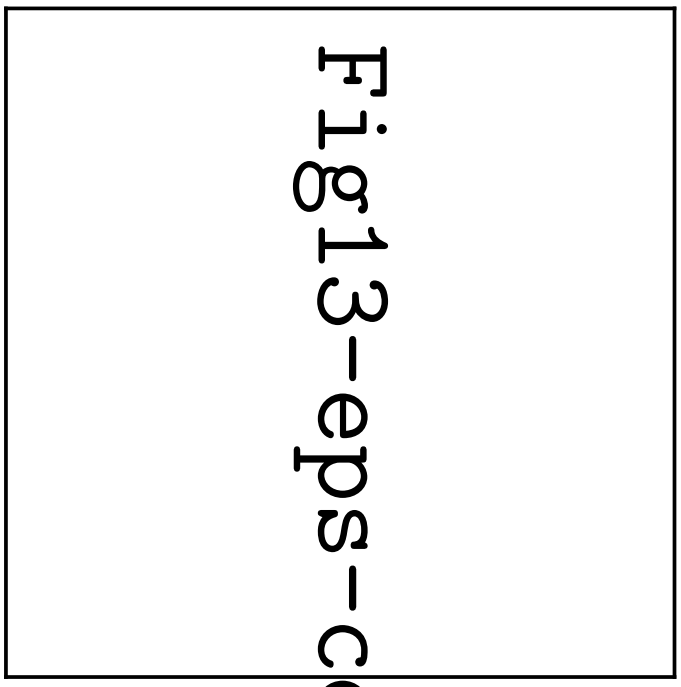

Figure 13 Same as Fig. 5 but for the $^{120}\mathrm{Sn}(p,p'x)$ reaction at 28.8 MeV.

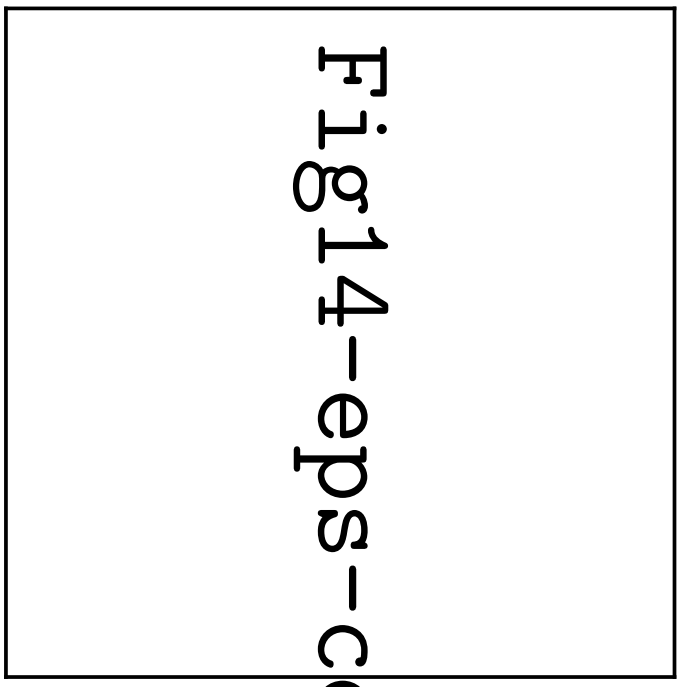

Figure 14 Same as Fig. 5 but for the ^{27}Al$(p,p'x)$ reaction at 62 MeV.

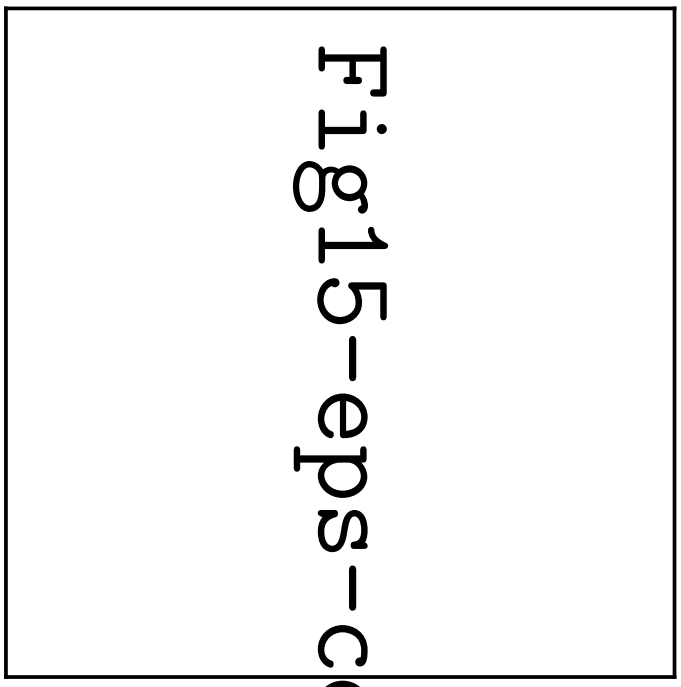

Figure 15 Same as Fig. 5 but for the $^{12}\mathrm{C}(p,p'x)$ reaction at 62 MeV.